

In-plane prestressed hair clip mechanism for the fastest untethered compliant fish robot

Zechen Xiong¹, Liqi Chen², Wenxiong Hao², Pengfei Yang³, Shicheng Wang², Sarah Li Wilkinson², Yufeng Su², Xiangyi Ren², Nipun Poddar², Xi Chen¹, Hod Lipson^{2,*}

¹*Department of Earth and Environmental Engineering, Columbia University, New York, NY 10027, USA*

²*Department of Mechanical Engineering, Columbia University, New York, NY 10027, USA*

³*School of Mechanical Engineering and Automation, Fuzhou University, Fuzhou 350108, China*

**Correspondence: hod.lipson@columbia.edu*

Abstract

A trend has emerged over the past decades pointing to the harnessing of structural instability in movable, programmable, and transformable mechanisms. Inspired by a steel hair clip, we combine the in-plane assembly with a bistable structure and build a compliant flapping mechanism using semi-rigid plastic sheets and installed it on both a tethered pneumatic soft robotic fish and an untethered motor-driven one to demonstrate its unprecedented advantages. Designing rules are proposed following the theories and verification. A two-fold increase in the swimming speed of the pneumatic fish compared to the reference is observed and the further study of the untether fish demonstrates a record-breaking velocity of 2.03 BL/s (43.6 cm/s) for the untethered compliant swimmer, outperforming the previously report fastest one with a significant margin of 194%. This work probably heralds a structural revolution for next-generation compliant robotics.

Summary: a new mechanism that heralds the structural revolution for high-performance compliant robotics.

Keywords: soft robotics, in-plane prestressing, compliant mechanism, bistable and multi-stable mechanisms

Main Text

Introduction

Bistable and multi-stable mechanisms are widely found in nature and human society to fulfill some rapid and repetitive tasks like hunting, locomoting, and fast deforming (1). These mechanisms achieve large shape transitions in a short amount of time while being elastic and reversible, thus are useful for programmable materials, morphing structures, and novel applications spanning several orders of magnitude (2). On the other hand, pre-stressing, similar to how pre-tensioning offers mechanical benefits to civil engineering projects, helps make the most of the materials in morphing structures by elevating the stress level and increasing the elastic energy released and its releasing rate in each actuation. Examples of prestressing and multi-stability are not uncommon. Many plants can build up elastic energy through osmosis and turgor pressure. A sudden release of this energy can cause rapid movements and plays a critical role in

their functions like reproduction and nutrition: the ballistic seed dispersal of Impatiens and squirting cucumber after prestressing their seedpods (3); the pollen dispersal of trigger plants (4); the rapid leaf closure of Venus flytrap (5), etc. This prestress-and-snap mechanism is also observed in the animal kingdom. Birds use the prestressed tendon to play zero-powered perching (6) and the hummingbird's beak is a bistable structure that is capable of fast closure in the air by snapping (7). Combining prestressed structures with bistable mechanisms seems to be a potential option for fast morphing and robotic locomotion.

Compared to traditional robotic mechanisms made of rigid links and joints, soft mechanisms are safe, versatile, more bio-mimic, and bio-compatible because of the elastic and compliant materials used, but are intrinsically weaker in force exertion and fast-moving (8, 9). The moduli of soft materials are usually in the order of 10^4 - 10^9 Pa (10), yet if only the material has a high level of elasticity, it can be used for compliant mechanisms. In many cases of soft robots, large blocks of elastomer for self-supporting and end-effectors leads to a comparatively low energy density (10); the widely used fluidic actuation also dissipate too much energy in viscous friction with the tube, especially when the actuation frequency is high (11). To address these, about three potential solutions are proposed: larger energy input, higher frequency, and using structural instability. For example, Shepherd et al. (12), Bartlett et al. (13), Tolley et al. (14) and Keithly et al. (15) used explosive actuators to power jumping robots. These robots usually move fast and in a very uncontrollable pattern. Besides, the soft materials accommodating the explosive impact degenerate rapidly after a few repetitions. Mosadegh et al. (16), Huang et al. (17), Li et al. (18), and Wu et al. (19) designed soft robots with high actuation speed or frequency. Due to the low moduli of elastomers, fast and high-frequency actuation usually contradicts soft robots, hindering their use. By introducing instability, Tang et al. (20) built a galloping soft robot with a speed of 2.68 body length per second (BL/s) and a soft swimmer of 0.78 BL/s. Other researches (11, 21, 22) also point to the potential of multi-stable structures leading the next-generation soft robotics. However, presently reported multi-stable structures are still complex in constitution, assembly, and fabrication processes, impeding their development. The method illustrated in this work proposes to create strong bi-stable mechanisms using prestressed 2D materials, which largely decrease the difficulty in design and fabrication.

Theory

Enlightened by buckling and post-buckling knowledge (23, 24) and the fact that most fast-moving animals in nature need a hard skeleton, we demonstrate in Fig. 1A-G and movie S1 the geometry and assembly of a kind of hair-clip-like in-plane prestressed mechanism that is fabricated with materials like metal, plastic, and paper. Even though these materials are high in modulus, the out-of-plane stiffness of the slender ribbons made from them is usually smaller than the membrane stiffness by an order of 10^5 - 10^6 , making the ribbons compliant and deformable. By pinning the two extremities of the angled ribbon together with an eyelet rivet, the lateral-torsional buckling of the props (denoted by L_2) of the angled ribbon creates a thin-wall spatial surface with non-zero

Gaussian curvatures, i.e., a thin-wall dome. Displacement components u , v , and φ are measured on centroid C of an arbitrary section mn along x , y , and z axes (undeformed coordinates), respectively, with signs following the directions of axes and right-hand rule; the ξ , η , and ζ axes (deformed coordinates) are drawn through the deformed centroid C' of the section mn , coinciding with the principal axes of the deformed configuration. Following the small deflection theory and Euler's beam theory, and assuming the angled ribbon to be a straight cantilever beam of a rectangular section (Fig. 1D), the mathematical model of the assembly process can be given by the following equations (25):

$$EI_{\xi} \frac{d^2 v}{dz^2} + P(l - z) = 0 \quad (1)$$

$$EI_{\eta} \frac{d^2 u}{dz^2} + P\varphi(l - z) = 0 \quad (2)$$

$$C \frac{d\varphi}{dz} + P(l - z) \frac{du}{dz} - P(u_1 - u) = 0 \quad (3)$$

in which EI_i is the bending stiffness of the i axis, $l = L_1 + L_2$ is the half-length of the strip, $C = GJ = hb^3G/3$ is the torsional rigidity of the thin rectangular section mn , u_1 is the horizontal deflection at $z = l$, and G is the shear modulus. Considering the boundary conditions, the general solution of the above model is

$$\varphi = \sqrt{s} A_1 J_{1/4} \left(\frac{\beta_1}{2} s^2 \right) \quad (4)$$

with A_1 being a non-zero integration constant. This means the ribbon buckles approximately in the shape of a Bessel function. The calculation of A_1 and β_1 is explained in the supplementary information (SI), and the verification of Eq. (4) is done by comparing it to a corresponding finite element (FE) simulation illustrated in the SI and movie S2. Finally, by plugging Eq. (4) into Eq. (2), the out-of-plane bending angle ψ of the section mn can be calculated from

$$\psi \approx \frac{du}{dz} = -\frac{P_{cr}}{EI_{\eta}} \int_0^z \varphi(l - z) dz \quad (5)$$

with P_{cr} being the critical load of the lateral-torsional buckling of the angled ribbon. The above equation tells us that the tip bending angle ψ_l (Fig. 1H), a key factor for the kinematic performance of the hair clip mechanism (HCM), is independent of the material modulus E and dimensions like L_1 , L_2 , h , and t , but is only affected by the unitless shape factors θ and γ_s (Fig. 2C), if only the conditions are met that $h > 10t$ and the minor difference of Poisson's ratio ignored. The estimation of Eq. (5) gives an error smaller than 5% compared to the experimental measures with the bending sensor in fig. S2, as shown in Fig. 2A and 2B.

Assuming the snapping of an HCM is similar to that of an axially compressed beam as in Fig. 2D, the dimensionless energy barrier $\bar{U}_{barr} = U_{barr} L_1 / EI_\eta$ of the bi-states of the HCM can also be derived from the above inference (SI), which is

$$\bar{U}_{barr} \approx 3\bar{U} \Big|_{\psi_l = -\psi_{eq} \text{ or } \psi_{eq}} = 3P_{cr} \cdot L_2 \left(\sin^{-1} \frac{1}{\gamma_s} + \theta \right) \quad (6)$$

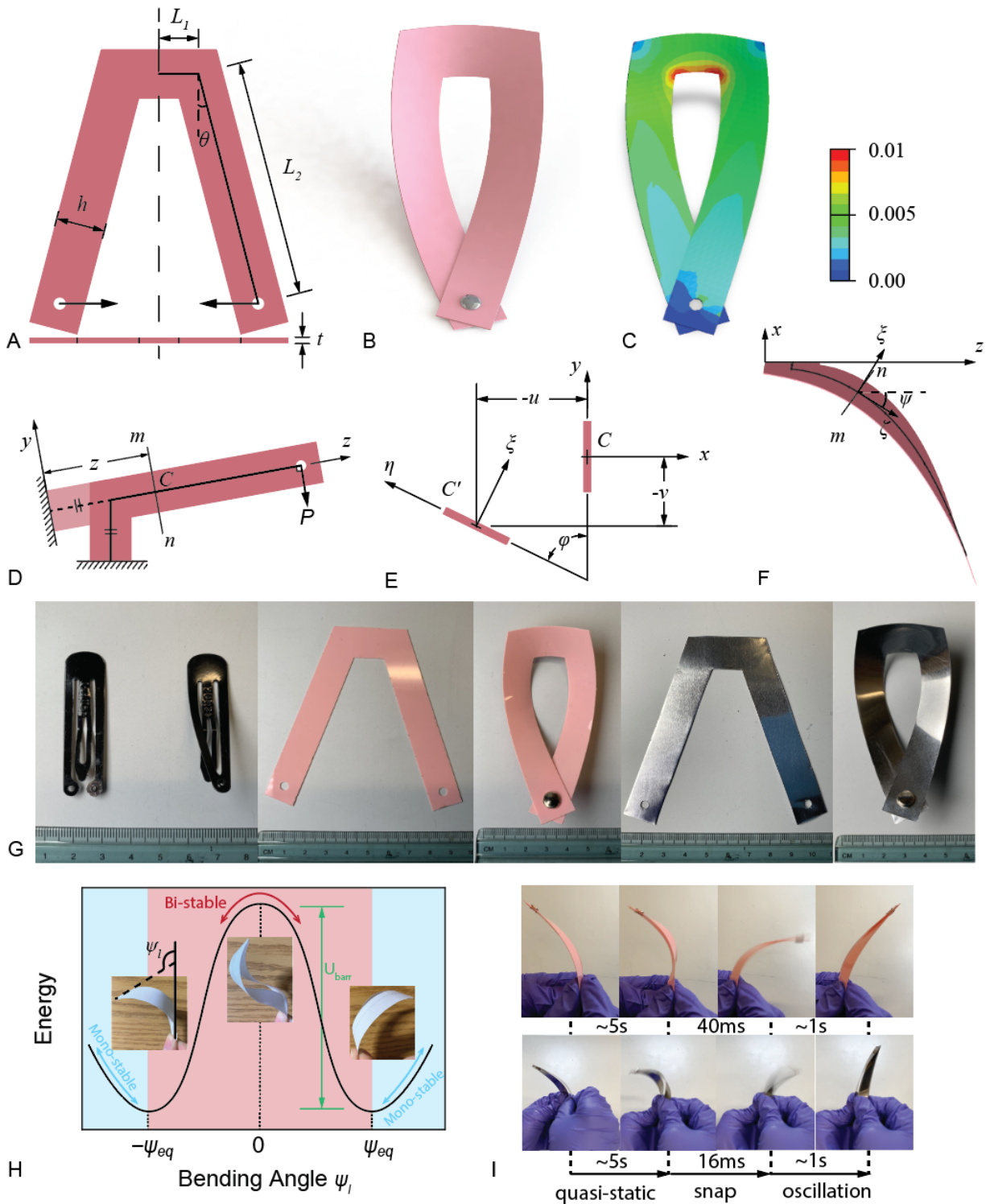


Fig. 1 **Design and mathematic modeling of in-plane prestressed hair clip mechanisms (HCM).** (A) The geometry of the ribbon before assembly. (B) and (C) Assembled configuration and corresponding contour of maximum principal strain, respectively. Shape factors $\theta = 10^\circ$ and $\gamma_s = L_2/L_1 = 6$; other parameters $h/L_1=15\text{mm}/12.5\text{mm}$ and $t/L_1 =$

0.381mm/12.5mm. **(D)** The "straightened" equivalent model for theoretic analysis. **(E)** The displacements of the section mn and **(F)** the configuration of the assembled HCM in the x - y plane. **(G)** A commercial hair clip as well as plastic and steel hair clips before and after assembly ($\theta = 20^\circ$ and $\gamma_s = 6$). **(H)** The energy profile and evolution of configuration of the snapping-through of a paper HCM. **(I)** The dynamics of snapping of a plastic and a metal HCM under a slow-mo camera ($\theta = 20^\circ$ and $\gamma_s = 6$).

A comparison between Eq. (6) and the corresponding FE simulations is shown in Fig. 2E. One of the simulated cases of HCM snap-through is given in movie S2 and the energy barrier is calculated from the difference between the maximum and minimum of its strain energy profile. In Fig. 2E, an error within 10% is observed. Again, the energy gap \bar{U}_{barr} also depends merely on the parameters θ and γ_s , indicating the scale-free nature of HCM. For example, increasing the thickness t by twofold doesn't change ψ_l and \bar{U}_{barr} , yet leads to an eight-fold rise in U_{barr} . These scalable features can inspire novel designs of morphing structures, metamaterial, and soft robots in both macro- and milli-scales.

The timescale t_* of HCM snap-through can be estimated as (26)

$$t_* = \frac{l^2}{t\sqrt{E/\rho_s}} \quad (7)$$

where ρ_s is the density of the material. The difference in timescales of HCM snapping is shown using different materials in Fig. 1G and movie S3. A plastic HCM with $\rho_s=1.2 \text{ g/cm}^3$, thickness $t = 0.381\text{mm}$, $E = 1.73 \text{ GPa}$ (SI), and $l = 175\text{mm}$ takes about 40 ms to snap and the angular speed is $\sim 4 \times 10^3^\circ/\text{s}$, while a steel HCM with $\rho_s=7.85\text{g/cm}^3$, $t = 0.254\text{mm}$, E about 200 GPa, and $l = 175\text{mm}$ only takes about 16 ms and have an angular speed of $\sim 14 \times 10^3^\circ/\text{s}$. The theory gives a good estimation. These velocities are comparable to those of the throws of a professional baseball player of $\sim 9000^\circ/\text{s}$ (27) and much faster than the tail beats of fish which is about $100\sim 1000^\circ/\text{s}$ (28). In the quasi-static energy-storing stage (Fig. 1I), the tip bending angle $|\psi_l|$ of an HCM further increases, and when it snaps, the total energy was released in several to tens of milliseconds, generating fast reverse swinging and small shock waves that result in a clear snap sound (movie S3). Excessive energy is then dissipated through oscillation.

We also noted that the global snap-through of the HCM can be triggered by the reverting of the central segment (denoted by L_1). This means HCMs can be triggered more conveniently by assorted actuation that offers a point displacement at one end, allowing the extruded long props (denoted by L_2) to be used as end effectors of robots or manipulators. This local-global actuation is termed as "bend-propagating actuation" in the relevant literature (22). With characteristics like bi-stability, easy actuation and fabrication, and scalability, we believe the in-plane prestressed HCM can be used in domains like origami/kirigami structure (29, 30), deployable devices (23, 31), morphing airfoils (32, 33), etc.

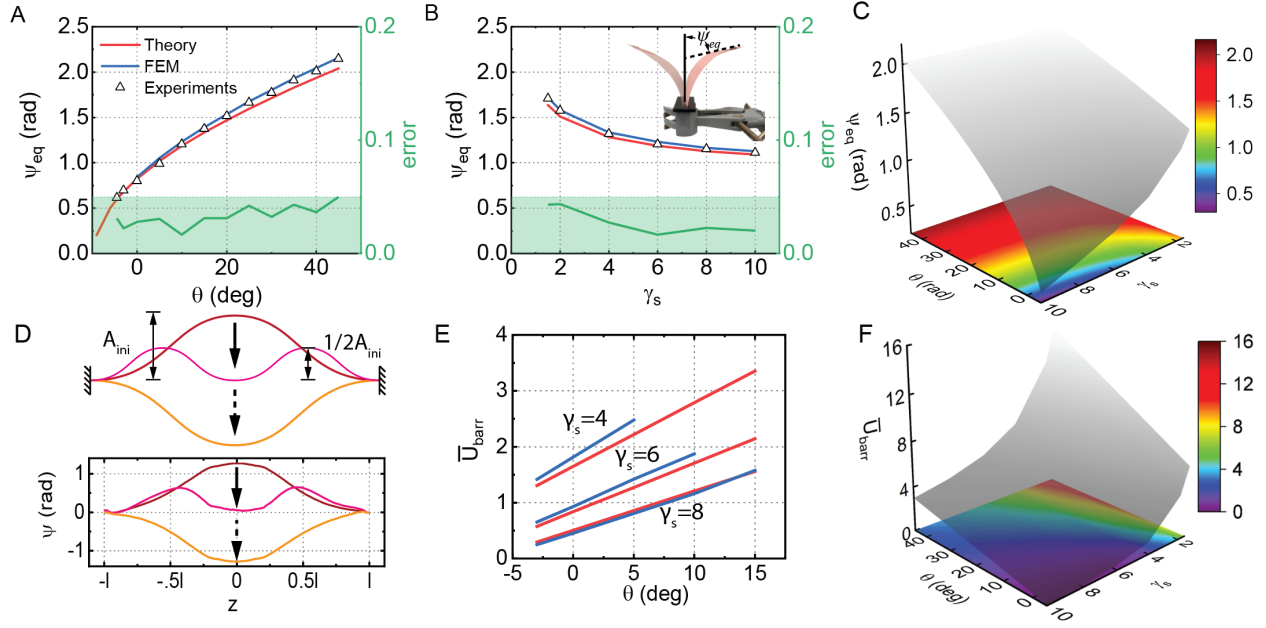


Fig. 2 Characterization of the pre-buckling and the post-buckling of HCMs. (A) and (B) Comparison of the value ψ_l among theoretic model, FE reproduction, and experiment results w.r.t. varying prop angle θ when $\gamma_s = L_2/L_1 = 6$ and dimensionless prop length γ_s when $\theta = 10^\circ$, respectively. The region within 5% error (calculated by comparing the theory to experiments) is highlighted in green. Inset shows the bi-states and tip bending angle ψ_l . (C) and (F) Maps illustrating the designing spaces of θ and γ_s , respectively, w.r.t. ψ_l and the unitless energy gap \bar{U}_{barr} . (D) Comparison of snap-through evolutions between the theory and the FE reproduction. A_{ini} denotes the deflection “amplitude” of a pre-buckled curve. (E) Comparison between theory and FE results of \bar{U}_{barr} w.r.t. shape factors θ and γ_s .

Pneumatic HCM for soft robotic fish and manipulators

Inspired by the undulating motion of the compliant body in fishes, we used an HCM in a pneumatic fish robot to demonstrate its superiority in locomotion. The composition of the minimalistic fish robot is illustrated in Fig. 3A. Its dimensions are length \times width \times height = 18.6cm \times 6.5cm \times 5.2cm (including fins) and is made of two major parts: a pneumatic HCM (pink, film thickness $t_1=0.381$ mm) with a riveted thinner plastic sheet (grey, film thickness $t_2=0.191$ mm) as compliant fish body and fish tail, and a hollow 3D-printed fish head to guide and balance the motion and accommodate any future control and energy systems. The HCM used in the fish has a shape of $\theta=-3^\circ$ and $\gamma_s=6$, which yield a tip bending angle $\psi_l = 39^\circ$ according to the theory. A pneumatic HCM is created by attaching a pair of antagonistic soft pneumatic bending units on both sides of the central area of the HCM. When gas is pumped into these pneumatic networks (pneu-nets), the bending deformation incurred will snap the mechanism. An alternate actuation of the pneu-nets would enable the HCM to undulate like a real fish. Silicone rubber and 3D-printed molds are used to cast the pneu-nets (details in SI). The thinner plastic sheet functions as a caudal fin to increase aquatic propulsion. An external pumping system (which isn't shown in the figure) works as both an energy source and control system, which also makes the fish robot a tethered one.

We noticed that by setting the equivalent density of the fish robot (total weight 42.5g) slightly larger than that of water via ballast (made of silicone rubber and steel balls), the robotic fish can move in a stable horizontal trajectory (movie S4 and movie S5). With an actuating pressure of 150kPa and a frequency of 1.3Hz (period = 760ms), the HCM-based bistable pneumatic soft robotic fish swims at an averaged underwater horizontal velocity of 26.54 cm/s (calculated from simple trigonometry), or 1.40 body length per second (BL/s), which is twice as fast as the monostable reference swimmer with the same weight (41.6g) and same actuation conditions (Fig. 3B and movie S4). The reference fish robot, instead of using bistable HCM for the fish body, features a flat and mono-stable plastic sheet with attached pneumatic bending units as actuators. The difference between these two models in speed can be identified clearer in Fig. 4 and movie S5. The pneumatic HCM fish can swim at a rate very close to the threshold of the swimming capacity of biological fishes (2 to 10BL/s (34)), and the single strike distance of the HCM fish robot is also comparable to that of a real fish (Fig. 4) yet the reference model only halves.

In Fig. 3C are depicted the kinematics of the two pneumatic fish robots, measured from high-fps videos (movie S5). A near-linear actuation swinging is observed in the reference swimmer, while the HCM-driven one shows nonlinear swinging and gains more kinetic energy from each flapping. This is because the drag force of fluids is proportional to the squared value of the flapping speed. Even though the HCM fish robot swings with a slightly smaller amplitude than the reference (Fig. 3C), its angular speed in water is $1200^\circ/\text{s}$ when its body snaps, about three times that of the reference model of $340^\circ/\text{s}$ in its linear swings. Compared to other prominent predecessors (18, 20, 34–36), our HCM fish not only excels in velocity per actuation frequency (fig. S3) but also triumphs in the simplicity of assembly and fabrication. The HCM-driven swinging can also be stronger if we increase either actuation frequency or the configuring parameter θ , yet may require a higher working pressure and decrease the energy efficiency due to larger loss in the pneumatic system. In movie S6, a pneumatic HCM with shape factors $\theta = -3^\circ$ and $\gamma_s = 6$ is undulating with an amplitude of $\pm 50^\circ$ and a frequency of 2.5Hz, and the actuation pressure required becomes 300kPa, which is two times the pressure in the 1.3Hz undulation. The critical pressure needed to snap such pneumatic HCMs is discussed in the SI (fig. S4) and the animation of FE results is shown in movie S2. From this fish robot, we demonstrated the strong dynamic performance of HCMs and their compatibility with smart soft actuators, which helps researchers develop soft swimmers that match biological locomotion speed. An untethered case is also discussed in the next section.

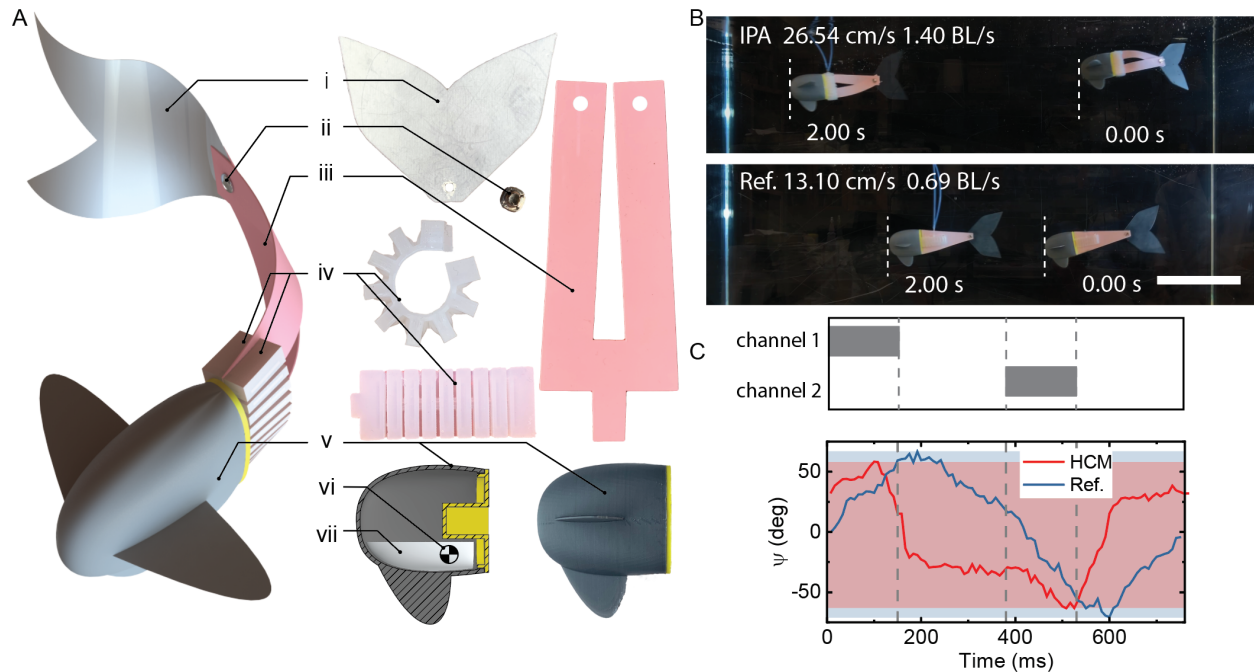


Fig. 3 Pneumatic HCM fish robot and its comparison with the reference model. (A) Assembly schematics of the robotic fish. i. caudal fin ($t=0.191\text{mm}$), ii. rivet pin, iii. HCM plate ($t=0.381\text{mm}$, $\theta=-3^\circ$, and $\gamma_s=6$), iv. antagonistic pair of pneumatic bending units (fabrication and dimension details shown in methods and Fig. S1), v. 3D-printed hollow fish head, vi. location of the mass center after assembly, and vii. casted ballast. (B) Comparison of underwater locomotion between HCM-based bistable fish robot and its monostable counterpart. Velocities are calculated from simple trigonometry. Scale bar, 150mm. (C) Comparison between the angular displacement ψ_i patterns of the two prototypes under 150kPa and 1.3Hz pressurization (period=760ms). Grey areas show when a channel is pressurized. The red and blue areas show the angular displacement range of the HCM and reference model, respectively.

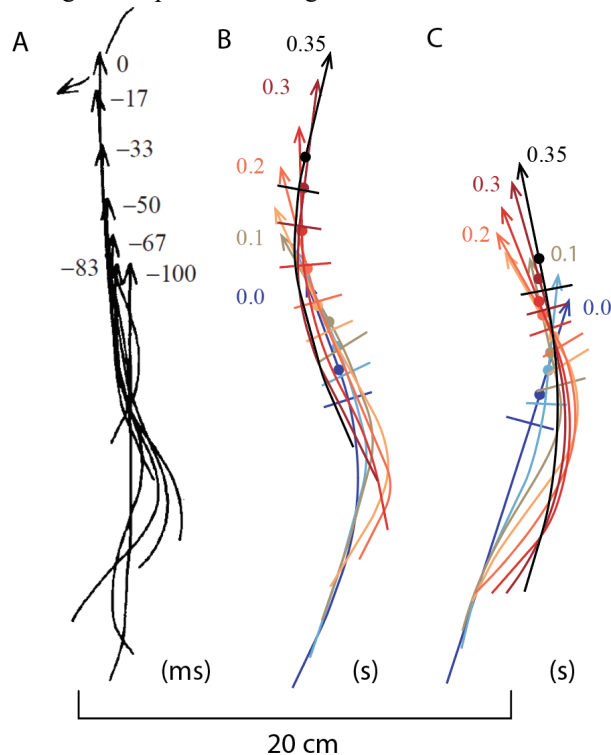


Fig. 4 **Comparison of strike patterns and sequences between biological and robotic fish.** (A) Strike pattern of a pike (*Esox* sp.) when hunting a smaller fish. Times are measured backward and in milliseconds. Reproduced from Webb and Skadsen (37). (B) and (C) Swimming sequences of body midlines and centers of mass (filled circles) in a single strike of the HCM-driven and the referential soft robotic fish, respectively. Short bars are the connection between fish heads and tails. Times are measured forward and in seconds.

Besides, to further demonstrate the versatility of HCM, we build a bistable soft gripper, as in Fig. 5. With a shape of $\gamma_s=6$ and $\theta=0^\circ$, and a tip bending angle of $\psi_l=47^\circ$, this HCM gripper can do human-like “pinching” grasps that pick up a piece of initially-flat soft fabric (Fig. 5A, 5B, and movie S7). This is because the HCM gripper has a nail-like geometry that can deal with tiny and deformable objects, while the lack of compliance in rigid grippers and the bulkiness of full-elastomer bodies in classic soft manipulators make them inappropriate for this task. The HCM bistable gripper has a payload several times its self-weight (Fig. 5C) and only consumes energy when a transition between releasing mode and grasping mode is needed. Researchers are utilizing similar theories to enhance grasping precision, reliability, and dexterity (38, 39), and the in-plane prestressed HCM in this work expands the spectrum.

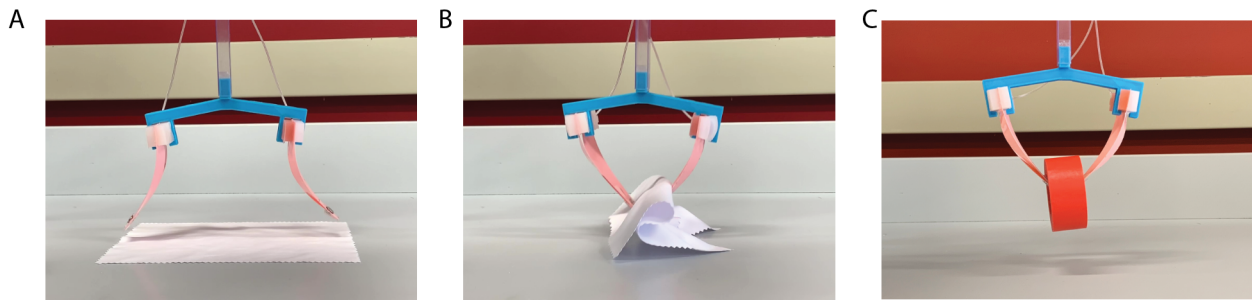


Fig. 5 **HCM-based bistable soft gripper.** (A) and (B) The Grasp of a thin and soft cloth. The shape factors of the HCMs used are $\gamma_s=6$ and $\theta=0^\circ$, providing a tip bending angle $\psi_l=47^\circ$. (C) The Grasp of a roll of tape (44g, total weight of the gripper: 15g).

Untethered Motor-driven HCM fish robot

Following the principles in the tethered pneumatic fish robot, an untethered motor-driven compliant fish robot is fabricated and tested in this section (Fig. 6). The hollow space of the fish head mentioned above is now utilized to host the Li-ion battery cells (3.7V, 350 mAh, 2-in-1 pack), a BLE microcontroller, a servo motor, and wiring stuff. The dimensions and weight of the untethered fish robot are length×width×height = 21.5cm×4.5cm×7.5cm and 125g, respectively. Contrary to the fact that untethering a soft robot usually decreases its swimming capacity (18), substituting the external actuation and control system with onboard ones enables our robot to explore further and at a higher speed. This is because the additional weight of the battery and controlling system in untethering has little influence on our design since we need weights and ballast to increase the density of the fish originally, and the mechanical actuation used is more powerful than soft actuation.

With a single servo motor powered by a 7.4V battery pack and a tail beating of 4Hz, the fish robot can move at an average speed of about 2.03 BL/s (43.6 cm/s), which is comparable to the speed of biological fish swimming. The fish can swim at a near-uniform circular motion with a radius of about 88.2 cm if we rivet the tail fin to the side of the two extremities instead of in the middle, providing clear images for the calculation of swimming speed. The measurement is conducted by comparing the distance covered in 1s time interval to the instantaneous length of the fish in the image (Fig.6C). It takes the robot about 12.7s to cover the circular path of 554 cm (movie S8) and the instantaneous speed is plotted in Fig. 6D. The speed is quite stable during this period, despite the variance of recorded values caused by turbulence as well as perspective distortion. This is the fastest untethered soft robotic swimmer, to the best of the authors' knowledge, outperforming the previously reported speed of 0.69 BL/s (18) by 194% and faster than most other tethered soft fish robots (fig. S4). This advantage would be even more significant if we consider speed in BL/s per actuation frequency. The comparison of the HCM motor-driven compliant fish is also illustrated in fig. S4.

On the other hand, the untethered fish, despite its faster absolute speed, is weaker in speed per frequency of actuation than the tethered one. This is because the HCM in the untethered model is fixed at the two vertices and actuated at the middle of the ribbon (Fig. 6) due to the single motor scheme, while the tethered fish is the opposite, which inevitably wastes more bending momentum of the fishtail in the untethered case. Also, the surface water drag and the total mass is proportional to the squared and cubed value of the fish dimension, respectively, making it disadvantageous to have a larger-sized fish robot. Interestingly, our fish doesn't scare away aquatic lives but arouses their curiosity sometimes (movie S8), which indicates its capacity for non-disruptive environmental exploring.

The setup in Fig. 6E and movie S9 demonstrates the measurement of propulsion force with varying flapping frequencies. A close-up demonstration of the high frequency of 2.5-4.0 Hz undulating of the HCM bi-stable fish body is given in movie S10. Typical curves of the forces are given in Fig. 6F and so is the averaged force w.r.t frequency measured during a period of 2s. A monotonous relation between force vs. frequency is observed and the fact that the slope of the curve is smaller in the low-frequency domain is probably due to the friction and inertia of the parts in the measuring setup. These features also indicate that the speed can be further increased with a higher snapping speed of the HCMs.

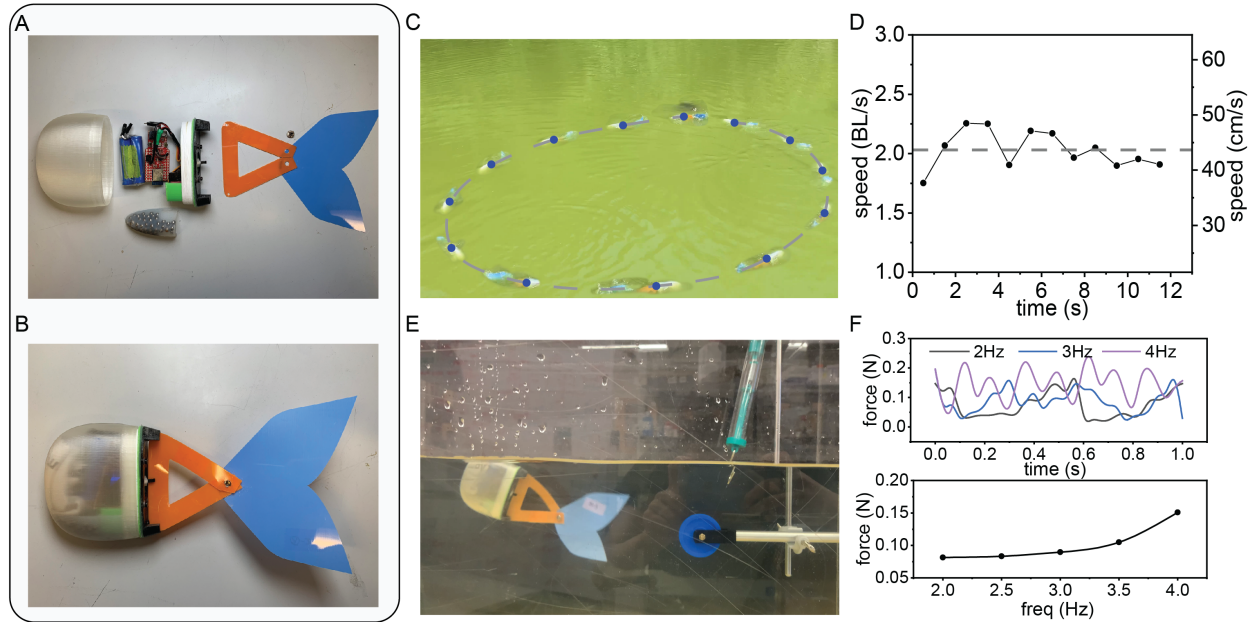


Fig. 6 Untethered Single Motor HCM compliant fish. (A) A breakdown of the robot. From left to right: 3D printed PLA shell, battery pack, cast ballast, BLE microcontroller, servo motor, PLA motor holder, silicone rubber waterproof, PLA connecting part, HCM body ($\gamma_s=2$, $\theta=-23.5^\circ$, and $\psi_l = 34^\circ$), rivet pin, and plastic tail fin. (B) Assembled robot. (C) The robot moves in a circle due to the asymmetric riveting at an average speed of 2.03 BL/s (43.6 cm/s). The snapshots of the fish are given at 1s intervals. (D) The speed curve of the fish in movie S8; values calculated in each second. The grey reference line at the value of 2.03 BL/s is the average speed of the whole period of 12.7s. (E) The setup for the measurement of the propulsion of the fish robot. (F) The typical curves of the propulsion of the fish under tail beat frequencies of 2Hz, 3Hz, and 4Hz, and the plot of averaged force during a 2s period w.r.t. tail beat frequency.

Conclusion

Harnessing the prestressing and bi-stability of 2D materials opens a new way to smart mechanisms with enhanced capability and functionality, inspiring applications in diverse fields and scales. Our research not only provides the principles for designing and fabricating such mechanisms inspired by the shape of a snap hair clip but also demonstrates the unprecedented functionality of HCMs as the propulsion part of fish robots. The configurable high force and high speed of the HCM give a two-fold increase in the speed of the pneumatic soft fish compared to the classic design and break the record for the untethered compliant swimmers with a significant margin of 194%. Without compromising the structural unity and cost competitiveness of soft robotics, this method has the potential of matching real fish speed with soft-bodied structure and initiating a structural revolution for the next-generation soft robotics.

References and Notes

1. Y. Chi, Y. Li, Y. Zhao, Y. Hong, Y. Tang, J. Yin, Bistable and Multistable Actuators for Soft Robots: Structures, Materials, and Functionalities. *Advanced Materials*. **34**, 2110384 (2022).
2. N. Hu, R. Burgueño, Buckling-induced smart applications: recent advances and trends. *Smart Mater. Struct.* **24**, 063001 (2015).
3. R. D. Deegan, Finessing the fracture energy barrier in ballistic seed dispersal. *PNAS*. **109**, 5166–5169 (2012).
4. P. E. Taylor, G. Card, J. House, M. H. Dickinson, R. C. Flagan, High-speed pollen release in the white mulberry tree, *Morus alba* L. *Sex Plant Reprod.* **19**, 19–24 (2006).
5. Y. Forterre, J. M. Skotheim, J. Dumais, L. Mahadevan, How the Venus flytrap snaps. *Nature*. **433**, 421–425 (2005).
6. A. Pal, D. Goswami, R. V. Martinez, Elastic Energy Storage Enables Rapid and Programmable Actuation in Soft Machines. *Advanced Functional Materials*. **30**, 1906603 (2020).
7. M. L. Smith, G. M. Yanega, A. Ruina, Elastic instability model of rapid beak closure in hummingbirds. *Journal of Theoretical Biology*. **282**, 41–51 (2011).
8. L. L. Howell, in *21st Century Kinematics*, J. M. McCarthy, Ed. (Springer London, London, 2013; http://link.springer.com/10.1007/978-1-4471-4510-3_7), pp. 189–216.
9. F. Ilievski, A. D. Mazzeo, R. F. Shepherd, X. Chen, G. M. Whitesides, Soft Robotics for Chemists. *Angewandte Chemie International Edition*. **50**, 1890–1895 (2011).
10. D. Rus, M. T. Tolley, Design, fabrication and control of soft robots. *Nature*. **521**, 467–475 (2015).
11. B. Gorissen, D. Melancon, N. Vasios, M. Torbati, K. Bertoldi, Inflatable soft jumper inspired by shell snapping. *Science Robotics*. **5** (2020), doi:10.1126/scirobotics.abb1967.
12. R. F. Shepherd, A. A. Stokes, J. Freake, J. Barber, P. W. Snyder, A. D. Mazzeo, L. Cademartiri, S. A. Morin, G. M. Whitesides, Using Explosions to Power a Soft Robot. *Angewandte Chemie International Edition*. **52**, 2892–2896 (2013).
13. N. W. Bartlett, M. T. Tolley, J. T. B. Overvelde, J. C. Weaver, B. Mosadegh, K. Bertoldi, G. M. Whitesides, R. J. Wood, A 3D-printed, functionally graded soft robot powered by combustion. *Science*. **349**, 161–165 (2015).
14. M. T. Tolley, R. F. Shepherd, M. Karpelson, N. W. Bartlett, K. C. Galloway, M. Wehner, R. Nunes, G. M. Whitesides, R. J. Wood, in *2014 IEEE/RSJ International Conference on Intelligent Robots and Systems* (2014), pp. 561–566.

15. D. Keithly, J. Whitehead, A. Voinea, D. Horna, S. Hollenberg, M. Peck, J. Pikul, R. F. Shepherd, A cephalopod-inspired combustion powered hydro-jet engine using soft actuators. *Extreme Mechanics Letters*. **20**, 1–8 (2018).
16. B. Mosadegh, P. Polygerinos, C. Keplinger, S. Wennstedt, R. F. Shepherd, U. Gupta, J. Shim, K. Bertoldi, C. J. Walsh, G. M. Whitesides, Pneumatic Networks for Soft Robotics that Actuate Rapidly. *Advanced Functional Materials*. **24**, 2163–2170 (2014).
17. X. Huang, K. Kumar, M. K. Jawed, A. M. Nasab, Z. Ye, W. Shan, C. Majidi, Chasing biomimetic locomotion speeds: Creating untethered soft robots with shape memory alloy actuators. *Science Robotics*. **3** (2018), doi:10.1126/scirobotics.aau7557.
18. T. Li, G. Li, Y. Liang, T. Cheng, J. Dai, X. Yang, B. Liu, Z. Zeng, Z. Huang, Y. Luo, T. Xie, W. Yang, Fast-moving soft electronic fish. *Science Advances*. **3**, e1602045 (2017).
19. Y. Wu, J. K. Yim, J. Liang, Z. Shao, M. Qi, J. Zhong, Z. Luo, X. Yan, M. Zhang, X. Wang, R. S. Fearing, R. J. Full, L. Lin, Insect-scale fast moving and ultrarobust soft robot. *Science Robotics*. **4** (2019), doi:10.1126/scirobotics.aax1594.
20. Y. Tang, Y. Chi, J. Sun, T.-H. Huang, O. H. Maghsoudi, A. Spence, J. Zhao, H. Su, J. Yin, Leveraging elastic instabilities for amplified performance: Spine-inspired high-speed and high-force soft robots. *Sci. Adv.* **6**, eaaz6912 (2020).
21. J. Sun, B. Tighe, J. Zhao, in *2020 IEEE International Conference on Robotics and Automation (ICRA)* (2020), pp. 10082–10088.
22. S.-W. Kim, J.-S. Koh, J.-G. Lee, J. Ryu, M. Cho, K.-J. Cho, Flytrap-inspired robot using structurally integrated actuation based on bistability and a developable surface. *Bioinspir. Biomim.* **9**, 036004 (2014).
23. Z. Xiong, H. Xiao, X. Chen, Fractal-inspired soft deployable structure: a theoretical study. *Soft Matter*. **17**, 4834–4841 (2021).
24. Y. Zhang, Y. Jiao, J. Wu, Y. Ma, X. Feng, Configurations evolution of a buckled ribbon in response to out-of-plane loading. *Extreme Mechanics Letters*. **34**, 100604 (2020).
25. S. P. Timoshenko, J. M. Gere, *Theory of Elastic Stability* (Courier Corporation, 2009).
26. M. Gomez, D. E. Moulton, D. Vella, Critical slowing down in purely elastic ‘snap-through’ instabilities. *Nature Phys.* **13**, 142–145 (2017).
27. N. T. Roach, M. Venkadesan, M. J. Rainbow, D. E. Lieberman, Elastic energy storage in the shoulder and the evolution of high-speed throwing in Homo. *Nature*. **498**, 483–486 (2013).
28. *Fish Swimming* (<https://link.springer.com/book/10.1007/978-94-011-1580-3>).

29. Y. Yang, K. Vella, D. P. Holmes, Grasping with kirigami shells. *Science Robotics*. **6**, eabd6426 (2021).
30. Y. Tang, G. Lin, S. Yang, Y. K. Yi, R. D. Kamien, J. Yin, Programmable Kiri-Kirigami Metamaterials. *Advanced Materials*. **29**, 1604262 (2017).
31. W. Wang, H. Rodrigue, S.-H. Ahn, Deployable Soft Composite Structures. *Scientific Reports*. **6**, 20869 (2016).
32. S. Daynes, K. D. Potter, P. M. Weaver, Bistable prestressed buckled laminates. *Composites Science and Technology*. **68**, 3431–3437 (2008).
33. S. Daynes, P. M. Weaver, Stiffness tailoring using prestress in adaptive composite structures. *Composite Structures*. **106**, 282–287 (2013).
34. R. K. Katzschmann, J. DelPreto, R. MacCurdy, D. Rus, Exploration of underwater life with an acoustically controlled soft robotic fish. *Science Robotics*. **3** (2018), doi:10.1126/scirobotics.aar3449.
35. A. D. Marchese, C. D. Onal, D. Rus, Autonomous Soft Robotic Fish Capable of Escape Maneuvers Using Fluidic Elastomer Actuators. *Soft Robotics*. **1**, 75–87 (2014).
36. Airacuda | Festo USA, (available at https://www.festo.com/us/en/e/about-festo/research-and-development/bionic-learning-network/highlights-from-2006-to-2009/airacuda-id_33879/).
37. P. W. Webb, J. M. Skadsen, Strike tactics of *Esox*. *Can. J. Zool.* **58**, 1462–1469 (1980).
38. L. U. Odhner, R. R. Ma, A. M. Dollar, in *2012 IEEE International Conference on Robotics and Automation* (2012), pp. 2830–2835.
39. J. Zhou, S. Chen, Z. Wang, A Soft-Robotic Gripper With Enhanced Object Adaptation and Grasping Reliability. *IEEE Robotics and Automation Letters*. **2**, 2287–2293 (2017).

Acknowledgments

We especially thank Yichao Tang and Jiahao Wu for their help with the experiments, Jiefeng Sun for the simulation suggestion, and all colleagues for the inspiring discussions. **Funding:** This work was supported by the Earth Engineering Center and the Center for Advanced Materials for Energy and Environment at Columbia University. **Author contributions:** Z. X. conceived the presented idea, developed the theory, built the simulation, and wrote the manuscript. Z. X., L. C., W. H., P. Y., S. W., S. L. W., Y. S., X. R., N. P. designed and carried out the experiments. X. C. and H. L. supervised the project. **Competing interests:** There are no conflicts of interest to declare. **Data and materials availability:** All data are available in the manuscript or supplementary materials.